Earth and Planetary Science Letters 488 (2018) 14–26

Contents lists available at ScienceDirect

Earth and Planetary Science Letters

www.elsevier.com/locate/epsl

Rayleigh and S wave tomography constraints on subduction termination and lithospheric foundering in central California ☆

Chengxin Jiang [a,*], Brandon Schmandt [a], Steven M. Hansen [a], Sara L. Dougherty [b], Robert W. Clayton [c], Jamie Farrell [d], Fan-Chi Lin [d]

[a] Department of Earth and Planetary Sciences, University of New Mexico, Albuquerque, NM 87131, United States
[b] Earthquake Science Center, U.S. Geological Survey, Pasadena, CA 91106, United States
[c] Seismological Laboratory, California Institute of Technology, Caltech 252-21, Pasadena, CA 91125, United States
[d] Department of Geology and Geophysics, The University of Utah, Salt Lake City, UT 84112, United States

ARTICLE INFO

Article history:
Received 3 November 2017
Received in revised form 2 February 2018
Accepted 6 February 2018
Available online xxxx
Editor: R. Bendick

Keywords:
Isabella Anomaly
San Andreas Fault
Sierra Nevada
Monterey microplate
lithospheric foundering

ABSTRACT

The crust and upper mantle structure of central California have been modified by subduction termination, growth of the San Andreas plate boundary fault system, and small-scale upper mantle convection since the early Miocene. Here we investigate the contributions of these processes to the creation of the Isabella Anomaly, which is a high seismic velocity volume in the upper mantle. There are two types of hypotheses for its origin. One is that it is the foundered mafic lower crust and mantle lithosphere of the southern Sierra Nevada batholith. The alternative suggests that it is a fossil slab connected to the Monterey microplate. A dense broadband seismic transect was deployed from the coast to the western Sierra Nevada to fill in the least sampled areas above the Isabella Anomaly, and regional-scale Rayleigh and S wave tomography are used to evaluate the two hypotheses. New shear velocity (Vs) tomography images a high-velocity anomaly beneath coastal California that is sub-horizontal at depths of ~40–80 km. East of the San Andreas Fault a continuous extension of the high-velocity anomaly dips east and is located beneath the Sierra Nevada at ~150–200 km depth. The western position of the Isabella Anomaly in the uppermost mantle is inconsistent with earlier interpretations that the Isabella Anomaly is connected to actively foundering foothills lower crust. Based on the new Vs images, we interpret that the Isabella Anomaly is not the dense destabilized root of the Sierra Nevada, but rather a remnant of Miocene subduction termination that is translating north beneath the central San Andreas Fault. Our results support the occurrence of localized lithospheric foundering beneath the high elevation eastern Sierra Nevada, where we find a lower crustal low Vs layer consistent with a small amount of partial melt. The high elevations relative to crust thickness and lower crustal low Vs zone are consistent with geological inferences that lithospheric foundering drove uplift and a ~3–4 Ma pulse of basaltic magmatism.

1. Introduction

Transition of the western North America plate boundary from subduction to transform swept northward across central California during the Miocene fundamentally altering the tectonic and magmatic processes that shaped the crust and upper mantle structure in the region (Atwater and Stock, 1998). The modern seismic structure beneath central California is hypothesized to reflect these events, including remnants of subduction termination (Brocher et al., 1999; Wang et al., 2013), the post-subduction evolution of the continental volcanic arc that gave rise to the Sierra Nevada batholith (Zandt et al., 2004; Jones et al., 2014), and ~300 km of right-lateral transport of continental crust (Ducea et al., 2003; Ford et al., 2014). Distinct origins for some seismically detected structural heterogeneities in the deep crust and upper mantle have been proposed. A prominent example is the Isabella Anomaly, which is a high-seismic-velocity volume in the upper mantle centered beneath the southern Great Valley at ~100 km depth.

The Isabella Anomaly is a long-recognized seismic feature of the California upper mantle (Raikes, 1980; Biasi and Humphreys, 1992; Benz and Zandt, 1993), and there are two main types of hypotheses for its origin. The first posits that the Isabella Anomaly results from gravitational instability of compositionally dense lithosphere

☆ Any use of trade, firm, or product names is for descriptive purposes only and does not imply endorsement by the U.S. Government.

* Corresponding author.
E-mail address: chengxinjiang@gmail.com (C. Jiang).

https://doi.org/10.1016/j.epsl.2018.02.009
0012-821X/

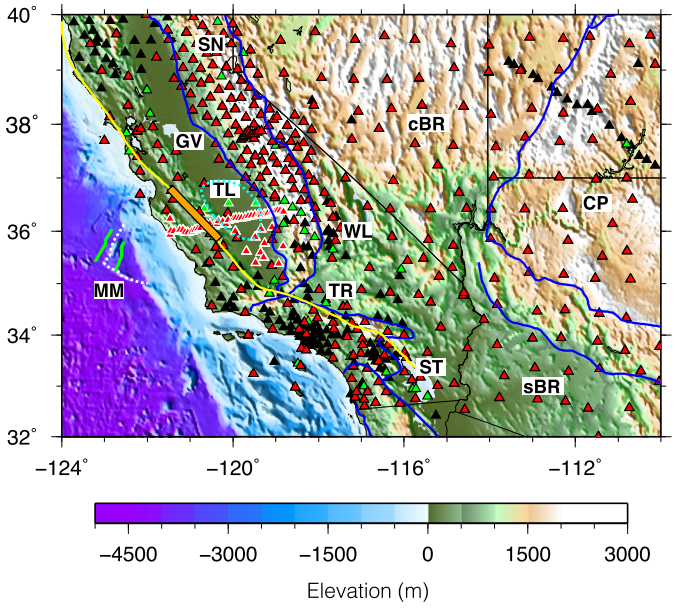

Fig. 1. Regional geography and station map. Major geological provinces of the region are outlined by thick blue lines and are labeled with abbreviated names, including Sierra Nevada (SN), central Basin and Range (cBR), southern Basin and Range (sBR) and Colorado Plateau (CP). The locations of some other major tectonic provinces that are referred in the text are also labeled in the map, including the Great Valley (GV), Walker Lane (WL), Transverse Ranges (TR) and Salton Trough (ST). The cyan dashed line delineates the Tulare basin (TL), referred in section 4.4 of the main text. The thick yellow line delineates the San Andreas Fault (SAF), and the orange rectangular box delineates the creeping section of the fault according to Moore and Rymer (2007). The green lines show the latest magnetic stripes (19–20 Ma) of the Monterey microplate (MM), which document the time that spreading ceased and the Monterey was captured by the Pacific plate (Lonsdale, 1991) and the white dashed lines delineate the western edges of the Monterey microplate. Triangles represent the stations used for both S-wave and surface wave data (red), used only for S-wave data (black) and only for surface wave data (green). The triangles with white outline represents the CCSE array. DOIs of these seismic networks are summarized in Table S1. (For interpretation of the references to color in this figure legend, the reader is referred to the web version of this article.)

generated beneath the southern Sierra Nevada batholith (Zandt et al., 2004; Boyd et al., 2004). Evidence for foundering of dense lithosphere includes: 1) the lack of a sufficiently thick crustal root to support 3–4 km elevations (Wernicke et al., 1996; Levandowski et al., 2013); 2) xenoliths and primitive basalts that indicate a thick column of mafic cumulates existed in the Miocene lower crust and uppermost mantle but was replaced by asthenosphere since ∼3–4 Ma (Ducea and Saleeby, 1996; Lee et al., 2001; Saleeby and Foster, 2004; 3) and geomorphic evidence for increased exhumation and river incision rates since ∼3–10 Ma (Clark et al., 2005; Sousa et al., 2017). Given the evidence for removal of lithosphere, the nearby high-velocity Isabella Anomaly beneath the Great Valley was suggested to be foundered arc lithosphere (Zandt et al., 2004; Boyd et al., 2004). However, questions remain regarding the westward location of the uppermost mantle anomaly with respect to the Sierra Nevada and why the anomaly has not sunk to greater depth (e.g., Zandt, 2003). These characteristics may be explained by a modest density anomaly of ∼0.5% (Levandowski and Jones, 2015) and a pre-existing weak zone in the lower crust that would allow delamination to progress from east-to-west in the absence of other drivers of mantle flow (Le Pourhiet et al., 2006).

The second proposed origin for the Isabella Anomaly is a fossil slab fragment that remains attached to the Monterey microplate and is translating in the direction of Pacific plate motion beneath the western edge of North America (Wang et al., 2013; Pikser et al., 2012). The Monterey microplate is a remnant of the former Farallon plate that was captured by the Pacific plate at ∼19 Ma and resides offshore of central California (Fig. 1) (Lonsdale, 1991). The fossil slab is proposed to be a continuation of the Monterey microplate oceanic lithosphere that dips shallowly eastward under coastal California and steepens beneath the Great Valley accounting for the Isabella high-velocity anomaly (Pikser et al., 2012; Wang et al., 2013). A similar high-velocity anomaly is imaged landward of the Guadalupe and Magdalena microplates beneath the Baja peninsula suggesting that subduction termination just before local ridge-trench collision may favor preservation of fossil slab fragments (Wang et al., 2013). In central California, the possibility of a slab fragment underlying the continental crust landward of the Monterey microplate is suggested by the local absence of "slab-window" magmatism thought to represent slab removal elsewhere along the California coast (Wilson et al., 2005). Additionally, active source seismic imaging has tracked oceanic crust from offshore to beneath the California coast (Tréhu, 1991; Meltzer and Levander, 1991). However, the landward extent of the oceanic crust is not well constrained.

Thus, there is substantial evidence for both lithospheric foundering beneath the southern Sierra Nevada and a fossil slab at some distance inboard of the coast. What remains debated is the spatial extent and longevity of slab remnants and destabilized arc lithosphere in the shallow upper mantle. The conceptual model from Zandt et al. (2004) suggests that Monterey microplate crust extends to the San Andreas Fault (SAF) where it is truncated, and the Isabella Anomaly connects to the overlying plate beneath a cusp of thickened crust in the Sierra Nevada foothills. In contrast, the conceptual model from Wang et al. (2013) extends the Monterey microplate's fossil slab across the SAF where it dips to the east forming the Isabella Anomaly. In this context, the foundered lithosphere from beneath the Sierra Nevada has not been clearly identified seismically, suggesting it has sunk deeper or it is sufficiently small or similar in velocity to the surrounding mantle to avoid detection. Resolving the origin of the Isabella Anomaly has implications for understanding the spatial and temporal scales at which mafic cumulates are removed from the lithosphere (e.g., Kay and Kay, 1993; Jagoutz and Keleman, 2015) as well as the tectonic and dynamic consequences of ridge-trench collisions (e.g., Nicholson et al., 1994; Burkett and Billen, 2009).

In addition to consequences for long-term geologic processes, determining the Isabella Anomaly's origin has implications for along-strike variations in present plate boundary dynamics. The fossil slab hypothesis places subducted oceanic lithosphere beneath the section of the central SAF that dominantly deforms by aseismic creep (e.g., Titus et al., 2006) and hosts lower crustal seismic tremor and low-frequency earthquakes that can be triggered by small transient stresses (Peng et al., 2009; Shelly et al., 2009; Thomas et al., 2009). Frictional weakness of the central San Andreas is further indicated by maximum compressive stress orientations that are nearly orthogonal to the fault trace, consistent with low shear stress (Hickman and Zoback, 2004; Provost and Houston, 2001). Creation of a weak fault and near-lithostatic stress conditions have been linked to geochemical and magnetotelluric evidence for fluid input at the base of the crust (Kennedy et al., 1997; Fulton and Saffer, 2009; Becken et al., 2011), which provides a potential explanation for the talc-bearing serpentinites and Mg-rich clays found in the creeping section of the fault (Moore and Rymer, 2007; Lockner et al., 2011). Cooler temperatures and increased water content due to a fossil slab could enable prolonged dehydration and determine the limited along-strike extent of the creeping section (Pikser et al., 2012). A fossil slab may also explain a group of low-frequency earthquakes offset just east of the SAF at near-Moho depths (Shelly, 2015). Alternatively, geodynamic modeling has suggested that the flexural response to lithospheric instability beneath the southern Sierra Nevada could control the creeping section by creating a fault segment with near-lithostatic stress at typical seismogenic depths (Le Pourhiet and Saleeby, 2013).

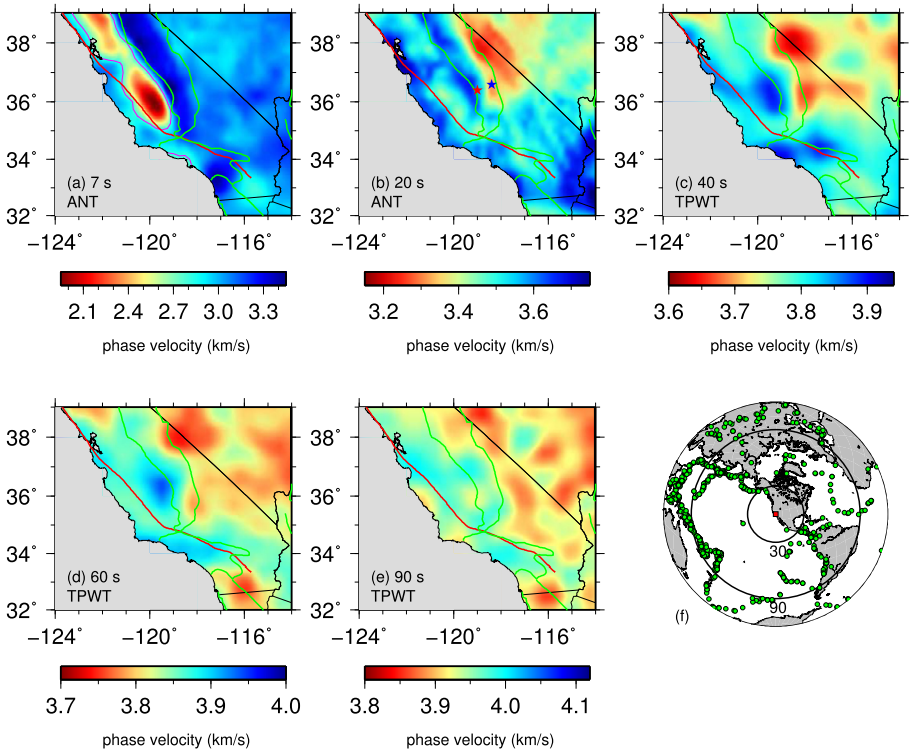

Fig. 2. Rayleigh wave phase velocity maps at various periods and the distribution of teleseismic events used for two plane-wave tomography (TPWT). The phase velocity maps at 7 (a) and 20 (b) s periods are based on ambient noise tomography (ANT), and those at 40 (c), 60 (d), and 90 (e) s periods are from TPWT. The two stars in (b) denote the locations referred to in Fig. 3. The red line delineates the San Andreas Fault, and the green lines outline major geological provinces. Note that the dashed purple lines in Fig. 2a delineates the 2.8 km/s contour referred in the text. (f) The map shows locations of teleseismic earthquakes used in the study. (For interpretation of the references to color in this figure legend, the reader is referred to the web version of this article.)

In order to investigate the origin of the Isabella Anomaly, a broadband seismic imaging project, the Central California Seismic Experiment (CCSE), was conducted in 2013–2015. While California is generally an area with outstanding seismic data coverage, the region directly above and west of the Isabella Anomaly had not previously been targeted by a dense broadband array. In this study, we used data from the CCSE array and surrounding regional networks deployed since 1997 (Fig. 1) to image shear velocity (Vs) structure of the crust and upper mantle with Rayleigh waves and teleseismic S body waves. The resulting improvements in crust and uppermost mantle resolution inform a reevaluation of structural remnants of subduction termination and foundering of continental arc lithosphere.

2. Data and methods

Seismic records including both continuous noise data and teleseismic earthquake data were collected from >400 broadband stations in the southwest United States (Fig. 1) operating between 1997 and 2015. The stations are mainly from three sources: the new CCSE array, permanent networks (CI, BK), and prior temporary arrays, including the Sierra Nevada EarthScope Project (SNEP) (Gilbert et al., 2012; Jones et al., 2014), the Sierra Paradox Experiment (SPE) (Boyd et al., 2004) and the EarthScope Transportable Array (TA) (Table S1). Ambient noise tomography and two-plane wave tomography (TPWT) were applied to obtain Rayleigh wave phase velocities at periods of 7–100 s. The resulting surface wave model was then used as a starting model for a joint inversion of Rayleigh wave phase velocities and teleseismic S wave travel times.

2.1. Rayleigh wave phase velocities from ambient noise

To obtain short-period phase velocity maps (7–25 s), a previously measured set of inter-station phase velocities from TA and permanent stations in 2005–2007 (Lin et al., 2008) was augmented with new inter-station noise correlation measurements for prior temporary arrays in the Sierra Nevada in 1997 and 2005–2007 and the CCSE array in 2013–2015. The time domain cross-correlation procedure described in Bensen et al. (2007) was followed except that the cross-correlations were computed in half overlapping 4-hour time windows (Seats et al., 2012) and each 4-hour cross-correlation was normalized by its maximum value. The frequency-time analysis method (FTAN) (Levshin and Ritzwoller, 2001) was used to measure the inter-station phase velocities. The cumulative set of phase velocity measurements were used in a ray-theory based tomographic inversion (Barmin et al., 2001) to obtain isotropic phase velocity maps (Fig. 2a–b). Because this inversion method does not estimate uncertainties, we used the averaged phase velocity uncertainties for the TA from Shen et al. (2013b) as our data uncertainties in subsequent Vs inversions.

2.2. Two-plane wave tomography with teleseismic earthquakes

About 770 earthquakes with Ms >5.5 and epicentral distance between 30° and 120° were selected for surface wave analysis (Fig. 2f). The FTAN method was used to isolate the fundamental Rayleigh wave on each seismogram and retrieve the phase and amplitude information. The TPWT method was applied to invert measurements of Rayleigh wave phase and amplitude for regional phase velocity maps at periods of 25–100 s (Forsyth and Li, 2005; Yang and Forsyth, 2006a). The tomographic inversion of the phase and amplitude measurements used 2-D finite-frequency sensitivity kernels derived by Zhou et al. (2004). The study region was parameterized with 0.5° grid spacing, and the velocity coefficients at the grid nodes are used to evaluate the phase velocity at finer resolution with a 2-D Gaussian weighted average of values at nearby grid nodes. Coefficients of uncertainty at each grid node were simulta-

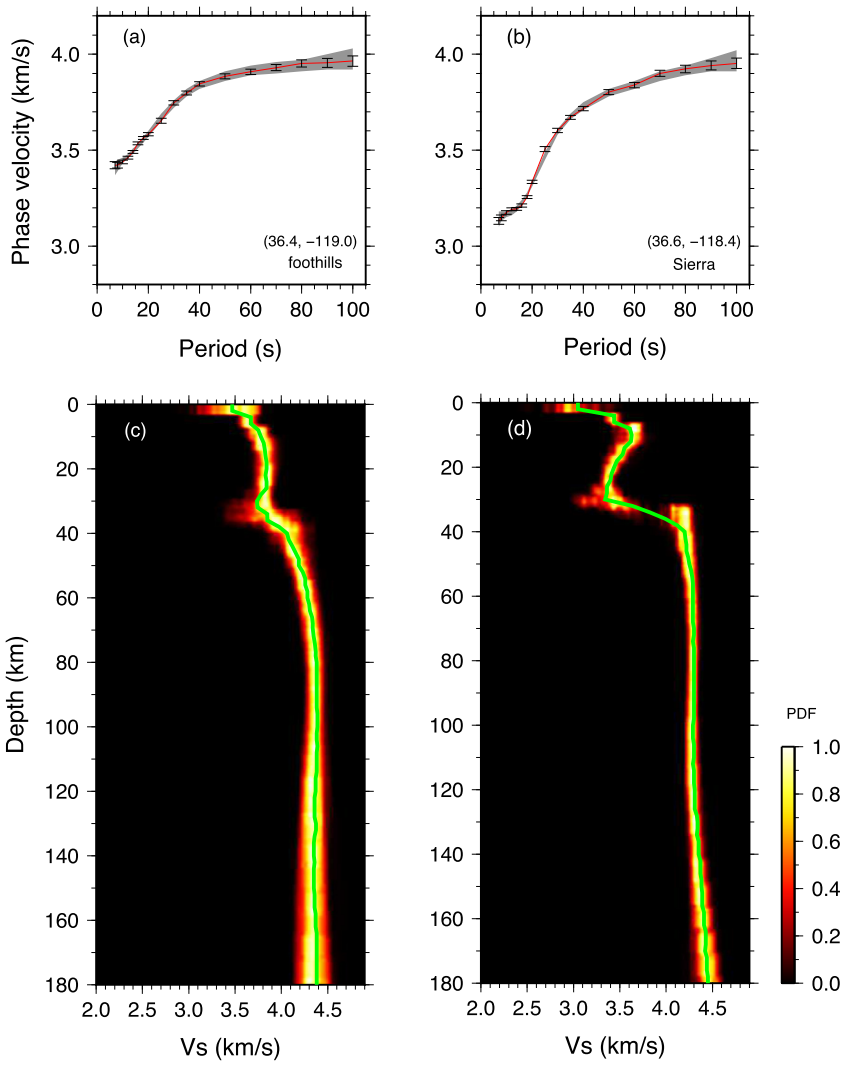

Fig. 3. Examples of 1-D Vs profiles from Bayesian Markov chain Monte Carlo (MCMC) inversion for locations in the western foothills (36.4, −119.0) and the eastern Sierra Nevada (36.6, −118.4). The two locations are identified by the red and blue stars in Fig. 2b and are referred to as "foothills" and "Sierra", respectively, in the main text. (a) Merged phase velocity dispersion curve (red line) at the western foothills from ANT and TPWT plotted with error bars and synthetic predictions (grey lines). The uncertainties of the phase velocity maps from ANT are scaled to make sure the one at the overlapping period of 25 s equals to that from TPWT. (b) Same as (a), but for the eastern Sierra Nevada. (c) Ensemble of 1-D Vs profiles inverted from the phase velocity dispersion curve in (a). The background color represents the normalized posterior probability density function (PDF). The green line shows the average of the posterior PDF, and is taken as our final 1-D Vs model for that grid point. (d) Same as (c), but for the eastern Sierra Nevada. The Moho depth from Tape et al. (2012) at the two profile locations are 36 km and 35.5 km, respectively (Fig. S1). (For interpretation of the references to color in this figure legend, the reader is referred to the web version of this article.)

neously estimated in the inversion (Fig. 3a–b). To ensure that the plane-wave assumption was satisfied, the study region was divided into four overlapping sub-regions. We first used all of the data to invert for average phase velocities across the region, and then updated the 2-D sensitivity kernels for regional phase velocity map inversions (Fig. 2c–e).

2.3. Probabilistic Rayleigh wave Vs tomography

The Bayesian Markov chain Monte Carlo (MCMC) inversion method of Shen et al. (2013a) was used to invert phase velocity dispersion curves from 7–100 s for 1-D Vs structure on a $0.2^\circ \times 0.2^\circ$ grid. At a period of 25 s, the noise and earthquake based phase velocity maps were averaged. The Vs inversion followed three main steps. First, a series of parameters were selected to represent the model space, and a prior distribution of the parameters was generated. Second, a Markov chain of candidate models was constructed with initial parameters randomly selected from the prior distribution. Candidate models were evaluated using the χ^2 misfit of the predicted dispersion curves, and model selection was guided by the Metropolis algorithm (Mosegaard and Tarantola, 1995). When an equilibrium in model misfit was attained a new Markov chain was formed by randomly sampling the model space again. The final posterior distribution that represents the solution of the inversion was formed by further selecting the models from the last step with χ^2 misfit smaller than a certain value, as done in Shen et al. (2013a, 2013b) (here the maximum χ^2 misfit is defined by the 200th best model, whose χ^2 value is usually between 1.0–1.3). This type of probabilistic inversion method has been widely used to invert seismic velocity models (e.g., Bodin et al., 2012; Shen et al., 2013b; Yao et al., 2010).

The model space is a set of 1-D Vs profiles extending from the surface to 250 km depth, which is represented by 10 or 11 parameters depending on the presence of a sedimentary layer. For points without a sedimentary layer, the model space is described by 10 parameters, including 4 B-spline velocity coefficients defining a continuous crustal Vs section, a parameter of crustal thickness and 5 B-spline velocity coefficients for the mantle above 250 km

Table 1
Model space for each model variable.

Model variable	Lower bound	Upper bound
Vs at top of sedimentary layer	0.5 km/s	2.5 km/s
1st B-spline coefficients of crust	2.5 km/s	3.8 km/s
2nd B-spline coefficients of crust	3.0 km/s	4.0 km/s
3rd B-spline coefficients of crust	3.0 km/s	4.2 km/s
4th B-spline coefficients of crust	3.0 km/s	4.4 km/s
Moho depth (relative to reference model)	−4 km	+4 km
1st B-spline coefficients of mantle	3.8 km/s	4.8 km/s
Deepest 4 B-spline coefficients of mantle	3.8 km/s	5.0 km/s

depth. An extra parameter representing the velocity at the surface is introduced for sedimentary basins, which were identified by 7-s period phase velocity <2.8 km/s (Fig. 2a). The absolute velocity of the surface and the first B-spline coefficient of the crust define a gradient layer down to 1/5 of the Moho depth. Introduction of the shallow gradient layer helps prevent falsely mapping large Vs anomalies occurring at the surface to greater depth.

The prior distribution of all parameters except the crustal thickness was a uniform velocity range. The purpose of a uniform prior is to reduce the dependence of the inversion on a starting model (e.g., Jiang et al., 2014; Shen et al., 2013a). Priors for all parameters are detailed in Table 1. Unlike the velocity parameters, the prior distribution for the Moho depth varied geographically. The model space for the Moho depth was a uniform range of ±4 km relative to a reference model from Tape et al. (2012) and Gilbert (2012) (Fig. S1a). Two additional prior constraints were imposed during model space sampling: 1) a positive Vs gradient was required immediately above and below the Moho; and 2) Vs <4.9 km/s was required at all depths. Inversions that allowed negative velocity gradients adjacent to the Moho resulted in some areas with thin anomalous Vs layers adjacent to the Moho, but the major features, such as the Isabella Anomaly, are similar (Fig. S2). Requiring positive gradients adjacent to the Moho was preferred in the inversion because it resulted in smoother models and still allowed resolution of a high-Vs lid overlying the asthenosphere in most of the region (e.g., Yang and Forsyth, 2006b).

During the inversion, Vp and density in the crust are scaled to Vs according to scaling relations 1 and 9 of Brocher (2005). Relative scaling relationships of $\delta \ln\alpha / \delta \ln\beta = 0.5$ and $\delta \ln\rho / \delta \ln\beta = 0.33$ (α is Vp, β is Vs, and ρ is density) (Panning and Romanowicz, 2006) were used to update the density and Vp in the mantle following Xing et al. (2016). Attenuation effects on surface wave dispersion were corrected following Kanamori and Anderson (1977) using PREM Q (Dziewonski and Anderson, 1981). Reasonable variations in the choice of Q model or empirical scaling relationships above would have minor effects on the resulting Vs models (e.g., Shen et al., 2013a).

After a comprehensive sampling of the model space (up to 300,000 iterations) from the prior distribution, the posterior distribution was obtained as described above at each geographic location on a 0.2° × 0.2° grid, and the mean and standard deviation were taken as our final Vs profiles and associated uncertainties, respectively. Finally, the 1D Vs profiles at all grid points were assembled to form a 3-D Vs model. Fig. 3 displays two examples of the 1D Vs profiles from the MCMC inversion.

2.4. Joint Rayleigh and S wave tomography

Teleseismic body wave tomography has relatively poor vertical resolution in the crust and uppermost mantle due to the steeply incident ray paths. By contrast, 7–100 s period Rayleigh waves are dominantly sensitive to structures from the upper crust to ~150 km depth, below which resolution begins to fade. The complementary sensitivity of S and Rayleigh waves to lithospheric structures makes a joint inversion a good option for improving resolution of the Isabella Anomaly, particularly at depths greater than ~100 km. For the joint inversion we updated the S-wave travel time data set used by Schmandt and Humphreys (2010a) with S and SKS measurements for the CCSE array. Relative travel times were measured using waveform cross-correlation (VanDecar and Crosson, 1990) in three frequency bands of 0.4, 0.1, and 0.05 Hz resulting in a total of >39,000 travel time measurements. These measurements were combined with the Rayleigh wave phase velocity maps described in the previous sections. Fig. 4 presents examples of S-wave residual times measured for the CCSE array as well as the surrounding permanent stations for two events from eastern back-azimuths. Note that the negative delay times indicative of the east-dipping high-velocity structure extend to near and in some cases just west of the SAF (Fig. 4).

The joint tomographic inversion scheme follows the approach of Obrebski et al. (2011), with minor modifications mentioned below. For the body wave component, the inversion uses the body wave travel time tomography method of Schmandt and Humphreys (2010a, 2010b), which relates travel time residuals to perturbations in velocity structure within the frequency-dependent volume of the first Fresnel zone. Sensitivities of the Rayleigh wave phase velocities to a 1-D Vs model and the predicted dispersion curves were calculated with the Computer Programs for Seismology package (Herrmann, 2013). In the forward calculations, density and Vp were scaled from Vs using the scaling relationships from the sur-

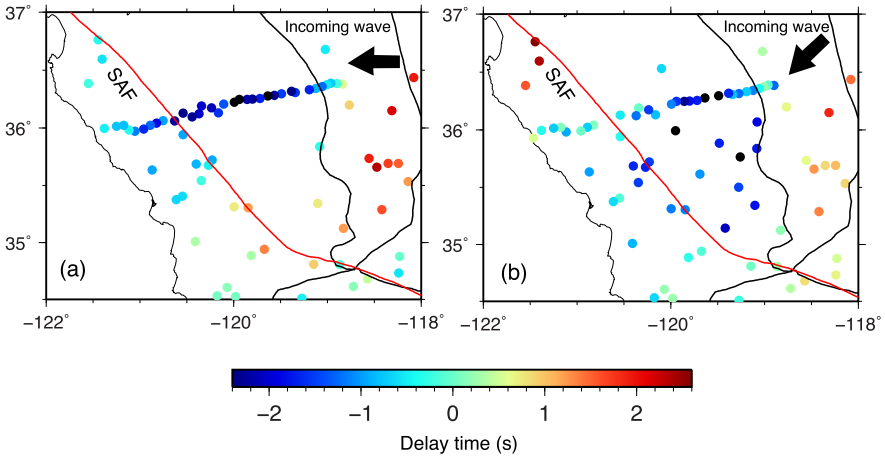

Fig. 4. S-wave residual times from two different teleseismic events recorded at CCSE and the surrounding permanent stations. The black arrows denote the azimuthal direction of the incoming S-wave. Note that the negative delay time across the CCSE array in Fig. 4a extend west of the Great Valley to near the SAF.

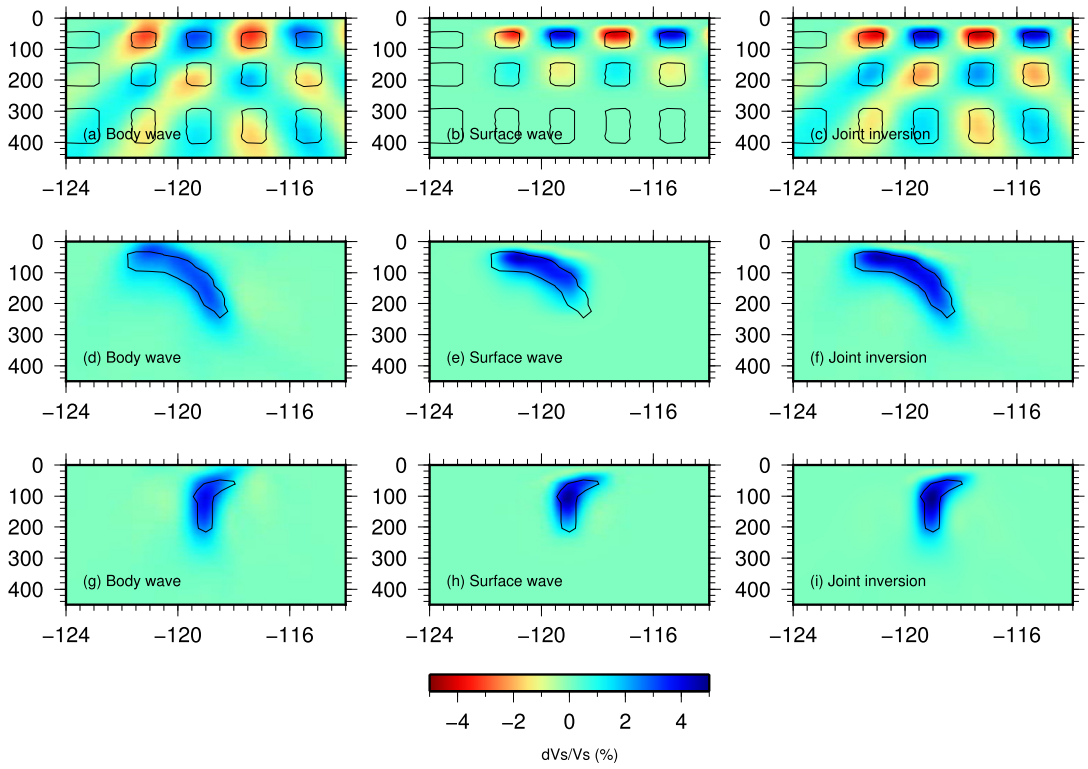

Fig. 5. Comparison of synthetic tests with body-wave data only (a), (d), (g), surface-wave data only (b), (e), (h) and joint inversion of body-wave and surface-wave data sets (c), (f), (i). The black line denotes the 3% contour of the input model. All the cross-sections are drawn along the latitude of 36°.

face wave inversion. Smoothing and damping regularization are included in the inversion (Schmandt and Humphreys, 2010a), and the linear inverse problem was optimized with the LSQR algorithm (Paige and Saunders, 1982). To allow the same model parameterization of Vs perturbation to be used for both data sets, the surface wave data were the residuals between the absolute phase velocities and predictions from the 1D model averaged across the study region based on the 3D Vs model from surface wave tomography. One difference from the approach of Obrebski et al. (2011) is that we damped the model perturbations relative to the 3-D Vs model derived from our surface wave inversion between 0 and 210 km depths underlain by an AK135 reference mantle (Kennett et al., 1995). We found this approach advantageous because the large crustal velocity variations needed to fit the short-period dispersion data were not recovered well if the LSQR inversion started from a 1-D Vs model. The crustal component of the 3-D starting Vs model was held fixed and the joint inversion was free to change the starting model beneath the Moho.

The model space in the joint inversion scheme is similar to that constructed in body wave tomography (e.g. Schmandt and Humphreys, 2010a), and consists of a series of nodes, between which the distance varies both laterally and vertically. The internode distance increases from 35 km in the center region covered by dense stations, to 60 km at the edge where there is a paucity of crossing rays. In the vertical dimension, the nodes are densely parameterized at the domain where both body and surface waves have sensitivities (10 km apart in the crust and 20 km below), and the vertical node spacing smoothly increases to 50 km by the maximum depth of 600 km.

A key component of the joint inversion is the relative weight assigned to each data set in the penalty function (e.g., Julia et al., 2000; Obrebski et al., 2011; Zhang et al., 2014). In this study, we select a relative weighting parameter by performing a trade-off analysis as outlined by Zhang et al. (2014). The body wave weight was fixed to be 1, and the surface wave weight was varied between 1 and 30. An optimal value of 8 was chosen from the resulting L-curve that reflects the variation of the two data misfits with the weighting parameter (Fig. S3). This value results in a comparable sensitivity of surface and body wave data to Vs at ∼60 km depth, with surface wave constraints becoming increasingly dominant at shallower depths and body wave constraints becoming dominant at greater depths. This weighting parameter accounts for effects of the different sizes and variances of the input data vectors and is the same as the ratio of $\frac{\alpha_i}{\beta_i}$ defined in eq. (10) of Julia et al. (2000). The results from another inversion with a weighting parameter of 12 for the surface wave data are presented in the supplementary information and changes to the resulting Vs model are generally <1% (Fig. S4 and Fig. S5).

2.5. Synthetic resolution tests

Three types of synthetic models are constructed to assess the resolution of the joint inversion algorithm and aid final model interpretation. The recovered checkerboard model (Fig. 5a–c) implies that introducing surface wave sensitivities to Vs structure improves resolution at depths less than ∼100 km, which is the primary domain of interest in this study. Body wave sensitivity to Vs improves recovery of features at depths >100 km compared to surface wave only inversions. In general, the joint inversion has the highest resolution at depths <100 km, and the resolution slightly decreases through the ∼100–300 km depth range. The recovery of input features deteriorates at depths >300 km, where the increasing length scales of sensitivity compromise recovery of ∼100 km scale features. The second synthetic test uses a hypothetical slab as the input (Fig. 5d–f) and shows that body wave data tend to distort the slab geometry by making it too steep. The surface wave tomography recovers the slab well at <100 km depth, but loses resolution at greater depths (Fig. 5e). The joint inversion algorithm improves recovery of the slab (Fig. 5f) by combining the complementary sensitivities of the two data sets. However, it should be

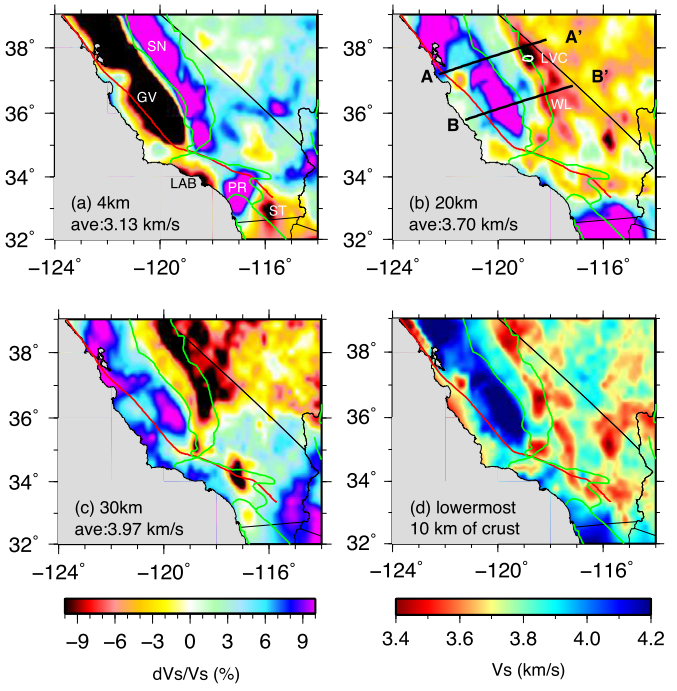

Fig. 6. Vs tomography maps from the Rayleigh wave Monte Carlo inversions at the depths of (a) 4, (b) 20, and (c) 30 km, respectively, plotted as perturbations relative to the regional average across the entire research area. The thick white line in (b) denotes the Long Valley Caldera according to Seccia et al. (2011). The two thick black lines in (b) show the locations of the transects in Fig. 7. (d) Vs averaged within the lowermost 10 km of the Moho, plotted as absolute values. The local Moho depth is defined by the average of the posterior distributions of crust thickness from the MCMC inversion (Fig. S1b). Other lines are as in Fig. 2. Abbreviations: GV—Great Valley, SN—Sierra Nevada, LAB—Los Angeles Basin, PR—Peninsula Ranges, ST—Salton Trough, LVC—Long Valley Caldera, WL—Walker Lane.

noted that the slab resolved by the joint inversion is still smeared horizontally and vertically, but to a lesser extent than in the body wave tomography. The final synthetic test contains a "drip-like" high-velocity feature beneath the Sierra Nevada (Fig. 5g–i) roughly following the qualitative drawing of Zandt et al. (2004). This test further indicates that the tomography is capable of distinguishing end-member fossil-slab and drip geometries.

3. Results

3.1. Crustal structure

The shallow crust (Fig. 6a) is characterized by low velocities in the Great Valley, Salton Trough, and Los Angeles Basin, and high velocities in the Sierra Nevada and Peninsular Ranges batholiths. In the middle-to-lower crust, the most prominent heterogeneity is a high-velocity anomaly, more than 10% faster than the regional average, beneath the Great Valley (Fig. 6b). The magnitude and geometry of this middle-to-lower crust high-velocity anomaly generally agrees with the Rayleigh wave tomography of Barak et al. (2015) and the full waveform tomography of Lee et al. (2014) in the areas where the models overlap. In the new Vs model, the Great Valley high-velocity anomaly is divided into southern and northern segments separated by more moderate Vs near 37.5° latitude (Fig. 6b), similar to lower resolution results using only TA data (e.g., Lin et al., 2014). The southern segment is mostly contained beneath the Great Valley, and the northern segment extends southwest from beneath the northern Great Valley to the San Francisco bay area.

Low velocity anomalies in the middle-to-lower crust are concentrated beneath the eastern Sierra Nevada and the Walker Lane (Fig. 6b). The strongest low velocity anomaly in the middle crust is closely aligned with the location of the Long Valley Caldera (Fig. 6b) and has Vs as low as ∼3.2 km/s. This feature has not been previously reported because it is largely constrained by the SNEP array and prior studies focused on longer period dispersion (Gilbert et al., 2012). Prior teleseismic P-to-S receiver function modeling for two stations near Long Valley Caldera found an ∼4 km thick low velocity layer centered at ∼9 km depth (Seccia et al., 2011). The new surface wave tomography images show a broader depth interval of ∼10–20 km, but that may result from coarser vertical resolution. The horizontal extent of the mid-crustal low Vs layer extends beyond the margins of Long Valley Caldera (Fig. 6b), which has a diameter of ∼15 km. However, the true extent is likely distorted by the 0.2° horizontal grid spacing.

At depths of ∼30 km, high-velocity areas are found beneath coastal California, the Great Valley, and from the Salton Trough into the southern Basin and Range (Fig. 6c). Along the coast and in the Salton Trough to southern Basin and Range these features result from shallow Moho depths of ∼20–25 km (e.g., Tape et al., 2012), which juxtapose uppermost mantle in these areas against lower crust beneath the Sierra Nevada, eastern Transverse Ranges, and the central Basin and Range. Beneath the Great Valley the Moho has a subtler Vs contrast because lower crustal Vs is $\geq$3.9 km/s (Fig. 6b–c), which is consistent with prior active-source P-wave constraints that indicate high-velocity lower crust (Vp ∼7.2 km/s) and Moho depths of ∼26–29 km (Holbrook and Mooney, 1987).

Velocities are relatively homogeneous in the upper and middle crust of the Sierra Nevada, but in the lower crust there is a well-defined contrast with lower velocities found beneath the higher elevation eastern Sierra Nevada (Fig. 6c–d). In the western Sierra Nevada, Vs averaged within the lowermost 10 km of the crust is ∼3.8–3.9 km/s, but the eastern Sierra Nevada and parts of the Walker Lane have slower and more variable mean lowermost crust Vs of ∼3.4–3.8 km/s (Fig. 6d). At 30 km depth, Vs beneath the eastern Sierra Nevada reaches as low as ∼3.25 km/s (Fig. 6c). Beneath the western Sierra Nevada foothills, we do not find an area of negligible Vs contrast (<0.1 km/s) across the Moho (Fig. 7), which was suggested by some prior receiver function studies (Zandt et al., 2004; Frassetto et al., 2011). The presence of at least a modest Vs increase (∼0.2 km/s) across the foothills Moho is consistent with recent full waveform and surface wave tomography (Lee et al., 2014; Barak et al., 2015) and a recent receiver function and surface wave study of crustal thickness that included prior temporary array data from the Sierra Nevada (Schmandt et al., 2015). The mean of the posterior crust thickness distribution from the MCMC inversion is similar to the regional model of Tape et al. (2012), which was taken as the center of the uniform likelihood prior distribution (Fig. S1). Our results do not provide evidence that major adjustments are needed, but we acknowledge that surface wave dispersion is only weakly sensitive to the Moho depth.

3.2. Upper mantle structure

Rayleigh wave only and joint inversion results for upper mantle depths are displayed in Fig. 8. The joint inversion mainly serves to extend resolution deeper into the upper mantle, which helps characterize the maximum depth of narrow heterogeneities like the Isabella Anomaly or the low-velocity anomaly beneath Long Valley Caldera. At depths less than ∼90 km the Rayleigh wave data provide better resolution and at depths greater than ∼130 km the S waves provide better resolution (Fig. 5). Both models are plotted in the transitional depth range of ∼90–130 km (Fig. 8). The upper mantle of California has a mean Vs of 4.26 km/s at 110 km depth, which is relatively low compared to the ∼4.5 km/s global

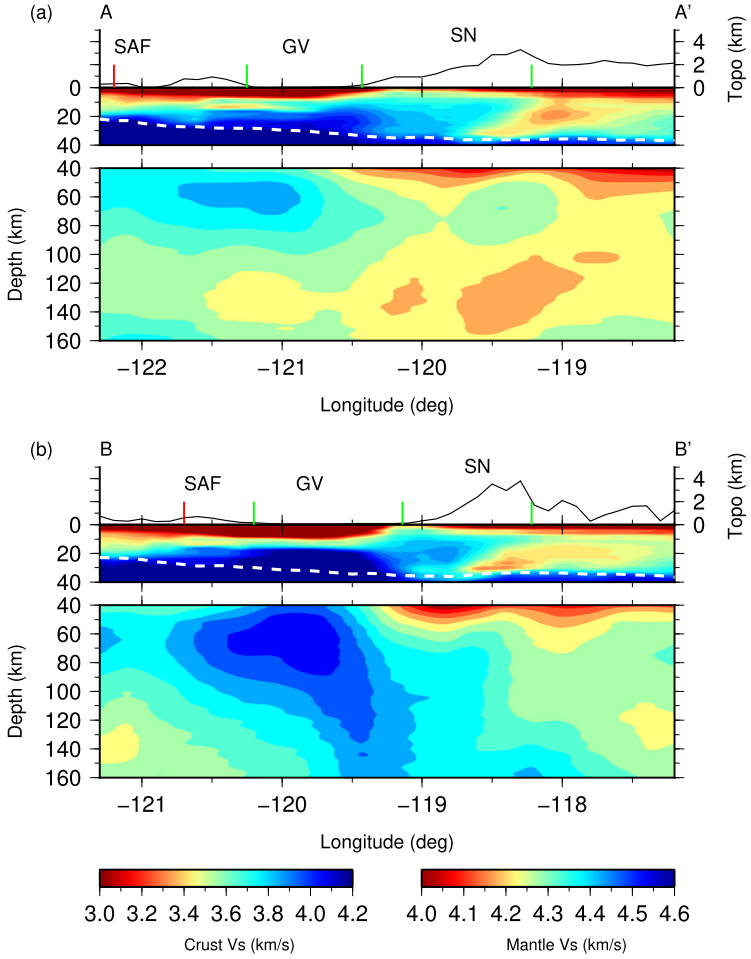

Fig. 7. Vertical cross-sections from the Rayleigh wave tomography model (Fig. 6) as absolute velocities along the two profiles marked in Figs. 6b and 8b from surface wave tomography only. The dashed white line illustrates the Moho variations along the sections from the MCMC inversion. Note that the crustal and the mantle components of the model are plotted with different color bars. The green line in the topography component delineates the San Andreas Fault (SAF), and the red lines delineate the geological boundaries for Great Valley (GV) and Sierra Nevada (SN). (For interpretation of the references to color in this figure legend, the reader is referred to the web version of this article.)

average (e.g., Yang and Forsyth, 2006b). However, considerable heterogeneities exist within the low velocity upper mantle.

Two concentrated low velocity anomalies with amplitude of >5% are observed in the upper mantle at ≤100 km beneath the Long Valley Caldera and the Coso Volcanic Field in the joint inversion results (Fig. 8e). In the Rayleigh wave only inversions, there is another similarly low velocity area beneath southern Nevada near the California border (Fig. 8a–b), but in the joint inversion model this area is comparable to the average within the central Basin and Range (Fig. 8e). The amplitudes of the Long Valley and Coso anomalies are diminished at depths >110 km. Both anomalies correspond to absolute Vs of ≤4.15 km/s at 60–90 km depth. The magnitude of these low velocity anomalies is greater in the models from joint inversion than those in the surface-wave only inversion, and the former is similar to the results from prior Rayleigh and S wave tomography (Wang et al., 2013).

Within the general low velocity upper mantle there are prominent high-velocity anomalies located beneath the southern Great Valley and the Transverse Ranges (Fig. 8). The Transverse Ranges anomaly straddles the 'big bend' in the SAF at ∼34° latitude and appears segmented into eastern and western components consistent with prior studies (Yang and Forsyth, 2006b; Schmandt and Humphreys, 2010a). The map-view images show that the center of the Isabella Anomaly gradually shifts from adjacent to the east side of the SAF at 60 km depth to beneath the southern Sierra Nevada at ∼150–190 km depth defining a clear eastern dip, consistent with azimuthal analysis of teleseismic delay times (Cox et al., 2016). The ∼40° east-northeast dip of the Isabella Anomaly is better illustrated in cross-section B-B′ (Figs. 7 and 9). The Isabella Anomaly has a horizontal extension west of the Great Valley beneath the coastal ranges of central California (Fig. 7), similar to the surface wave tomography results from Wang et al. (2013). The amplitude of the Isabella Anomaly diminishes at depths greater than ∼220 km (Fig. 9).

4. Discussion

4.1. Tectonic assembly of the southern Great Valley crust

The southern Great Valley middle-to-lower crust has anomalously high Vs of ∼3.9–4.2 km/s, in contrast to the anomalously low Vs of ∼3.2–3.4 km/s beneath the eastern Sierra Nevada at ∼30 km depth, and intermediate Vs beneath the western Sierra Nevada foothills (Fig. 6c, Fig. 7). The high Vs layer appears to shallow to the east and may reach the surface in the western foothills (Fig. 7). There is abundant active source seismic and potential field evidence for a west-dipping dense high-velocity layer that projects to the surface in the western Sierra Nevada foothills where a Mesozoic suture zone outcrops (e.g., Godfrey and Klemperer, 1998; Miller and Mooney, 1994). At the latitude of the CCSE line (∼36°), outcrops of the Kings–Kaweah ophiolite were emplaced in the early Jurassic by ∼190 Ma and modified by metamorphism and ig-

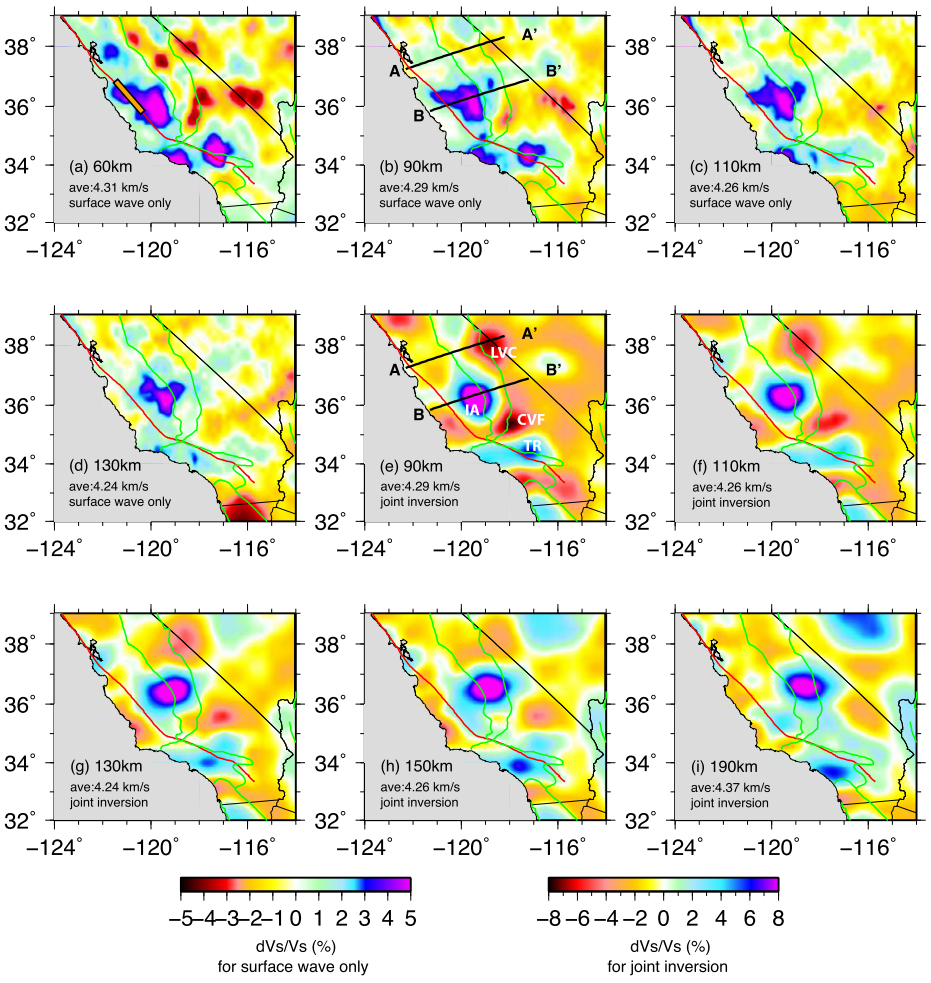

Fig. 8. Vs tomography maps at various depths of the upper mantle. (a)–(d) Vs tomography maps from surface wave inversion only. The maps are plotted as perturbations to the average velocity in the area shown at each depth, and the average value is marked in the SW corner of each figure. The orange rectangular box outlines the creeping section of the San Andreas Fault (SAF) according to Moore and Rymer (2007). (e)–(i) Vs tomography maps from the joint inversion. The two black thick lines in (c) and (e) show the locations of the transects in Figs. 7 and 9. Note that the color bars for the surface wave tomography and tomography from joint inversion are different, and the joint inversion models have larger amplitude of velocity variations than those from surface wave inversion only. Abbreviations: IA—Isabella Anomaly, TR—Transverse Ranges, LVC—Long Valley Caldera, CVF—Coso Volcanic Fields. (For interpretation of the references to color in this figure legend, the reader is referred to the web version of this article.)

neous intrusions during the late Jurassic Nevadan Orogeny (Saleeby and Sharp, 1980; Dickinson, 2008).

There are multiple hypotheses for how the exposed suture is related to the high-velocity layer at depth beneath the Great Valley. Miller and Mooney (1994) suggested the west-dipping subsurface interface is an intrusive shear zone with a modest velocity increase but strong deformational fabric. Based on the Vs tomography, the shear zone interpretation is viable in the uppermost ∼10 km beneath the foothills where Vs variations are subtle, but a major compositional contrast is necessary to explain the >0.5 km/s Vs increase with depth in the middle-to-lower crust beneath the Great Valley (Fig. 7). Alternatively, Godfrey and Klemperer (1998) and Fliedner et al. (2000) interpret the high-velocity layer as the projection of the foothills ophiolite to depth. Their interpretation is consistent with the high-Vs layer imaged here except that our model does not clearly recover the <10 km deep dipping interface. However, continuity of the ophiolite at depth is debated because drill cores that penetrate eastern Great Valley basement find Cretaceous (∼110–130 Ma) plutonic rocks more commonly than ophiolitic rocks (Saleeby, 2007). This poses an intriguing problem because the younger plutons would presumably have intruded through the pre-existing ophiolite. Reevaluation of the spatial relationships between the drill core data, geophysical transects including receiver functions from the CCSE array, and outcrop data appears warranted and will be the focus of a future study.

4.2. Sierra Nevada foothills crust and the Isabella Anomaly

It has been suggested that a v-shaped wedge of thickened and actively foundering crust beneath the western Sierra Nevada foothills is connected to the Isabella Anomaly thereby establishing its link to the batholith (Zandt et al., 2004). Most of this interpretation is based on receiver function analysis that indicated either an absence of a velocity contrast defining the Moho and/or a locally thickened cusp of ∼50–55 km thick crust whose Moho was not clearly imaged due to interface topography (Frassetto et al., 2011; Zandt et al., 2004). These characteristics were used to define an area of active foundering or a 'Moho hole,' which has become a target for geodynamic studies of the foundering process (e.g., Le Pourhiet et al., 2006; Valera et al., 2014).

The new Vs tomography does not indicate that actively foundering western foothills crust is connected to the Isabella Anomaly (e.g., Zandt et al., 2004) because the top of the Isabella Anomaly is imaged farther west (Fig. 7b). This result differs from tomography models that relied only on data from the Sierra Nevada

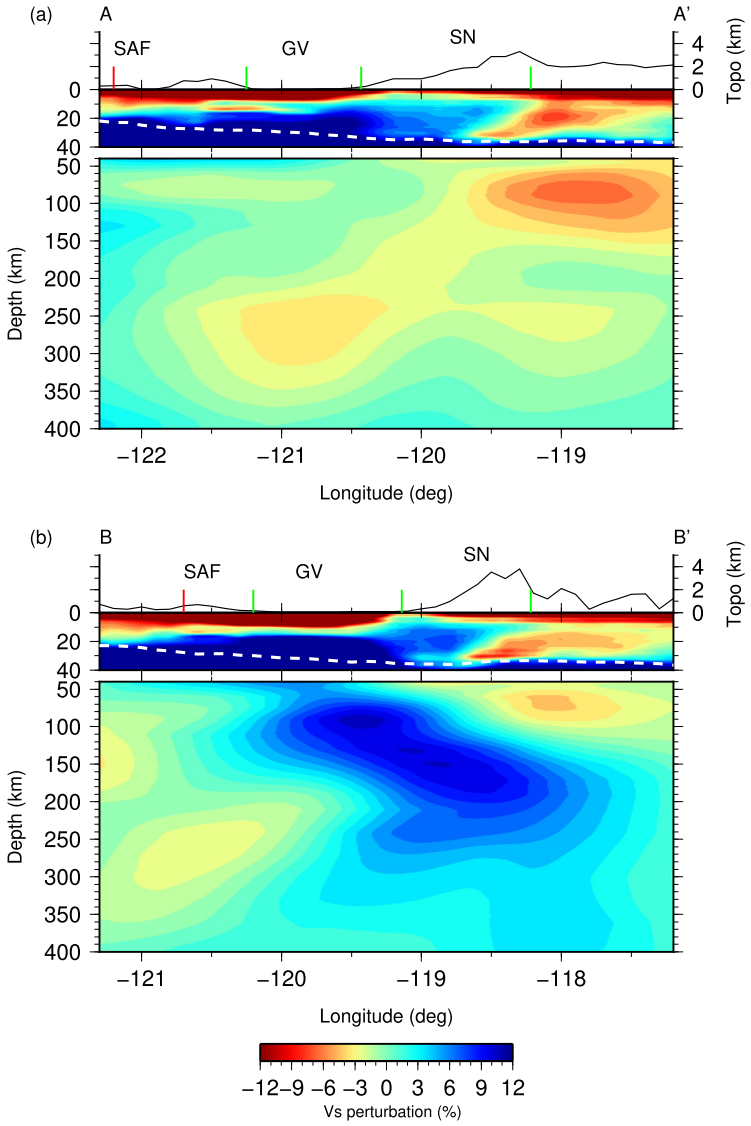

Fig. 9. Vertical cross-sections from the joint inversion model. The transects A-A′ and B-B′ are the same as in Fig. 7, but the mantle section is from the joint inversion. The dashed white line illustrates the Moho variations along the section from the MCMC inversion. Abbreviations: SAF—San Andreas Fault, GV—Great Valley, SN—Sierra Nevada.

(e.g., Boyd et al., 2004), but it is more similar to other models that included surface wave data from the TA (Barak et al., 2015; Wang et al., 2013; Jones et al., 2014). We caution that the presence of locally thickened crust beneath the foothills cannot be ruled out because detailed Moho structure is not constrained by surface wave tomography, and receiver function analysis from the full CCSE array is not yet complete. However, the position of the Isabella Anomaly in the mantle favors the interpretation that it is not connected to the Sierra Nevada foothills crust.

4.3. Lithospheric foundering beneath the high Sierra Nevada

Pliocene foundering of arc lower crust is supported by the coincidence of the eastward transition from the foothills to the high eastern Sierra Nevada where slightly decreasing crust thickness is coincident with the emergence of lower crustal low-velocity zone (Fig. 7b). A small fraction of mafic partial melt is a plausible origin for the low-Vs layer, which is consistent with high Vp/Vs estimates (Frassetto et al., 2011) and a ∼3–4 Ma pulse of mafic magmatism (e.g., Farmer et al., 2002). Depending on the assumed composition, the minimum Vs of ∼3.25 km/s in the lower crust likely corresponds to ≤4% melt (Watanabe, 1993; Chu et al., 2010), which could result from decompression melting of asthenosphere that rose to fill the void left by Pliocene foundering of density-unstable lower crust. Therefore, we propose that the slow lower crust and modest crust thickness (relative to the high elevations) marks the location of a lithospheric foundering event, which is similar to the interpretation of Frassetto et al. (2011) but with a more localized extent and a lack of connection to the Isabella Anomaly. Extension of the slow lower crustal velocities beneath the magmatically active Walker Lane could be linked to an eastward extension of foundering or focusing of asthenospheric melt into already thin Basin and Range lower crust as a result of the high rate of transtensional strain compared to the Sierra Nevada or interior of the Basin and Range (e.g., Kreemer and Hammond, 2007).

4.4. A fossil slab origin for the Isabella Anomaly

The sub-horizontal westward extension of the east dipping Isabella Anomaly from the Great Valley to beneath the coastal California and the lack of a connection to the lower crust of the

Sierra Nevada batholith lend support to the hypothesis that the Isabella Anomaly is a fossil slab fragment attached to the Monterey microplate (Figs. 7–8) (Benz and Zandt, 1993; Pikser et al., 2012; Wang et al., 2013). The structural connection of the Isabella Anomaly to the west of the Great Valley is further supported by preliminary receiver function imaging that finds an east-dipping interface in the uppermost mantle (∼35–80 km) just east of the SAF (Dougherty et al., 2017; Hansen et al., 2016). Our Vs tomography results show that at ∼60 km depth the center of the Isabella Anomaly is ∼100 km west of the lower crustal low velocity anomaly that we interpret to mark the location of Pliocene lithospheric foundering beneath the high Sierra Nevada. If the Isabella Anomaly is the dense actively foundering root of the batholith, then it is difficult to explain why its shallowest extent displaced so far to the west without sinking. Poor vertical resolution of teleseismic body wave tomography in the uppermost mantle (e.g., Boyd et al., 2004; Schmandt and Humphreys, 2010a) may largely be the origin of earlier interpretations that the Isabella Anomaly is connected to the western Sierra Nevada foothills. Recent teleseismic body wave tomography of the Cascadia subduction zone maps the Juan de Fuca slab ∼100 km too far inboard in the uppermost mantle where it appears to have a sub-vertical connection to arc or forearc crust (e.g., Schmandt and Humphreys, 2010b), unless additional constraints from surface waves (Obrebski et al., 2011) or regional body waves are used (Chu et al., 2012).

The evidence for the fossil slab origin highlights the need to reconsider or refine regional models of foundering of Sierra Nevada lithosphere, sedimentation in the Tulare basin of the southern Great Valley, and the origin of the creeping section of the SAF. A simple hypothesis for the structural remnants of lithospheric foundering beneath the eastern Sierra Nevada is that the removed volume is smaller than the Isabella Anomaly and has seismic velocities similar to the asthenosphere. For instance, mafic cumulates may have been removed as multiple small instabilities rather than migrating laterally to coalesce into a large instability (e.g., Jones et al., 2014). Subsidence documented by sedimentation in the Tulare basin has been attributed to active foundering of lower crust into the Isabella Anomaly (Saleeby and Foster, 2004). However, recent modeling of flexural isostasy is consistent with a modest density anomaly of ∼0.2–0.5% in the Isabella Anomaly (Levandowski and Jones, 2015). If such a subtle density anomaly is plausible, we suggest that origins other than foundered mafic cumulates from beneath the Sierra Nevada should be considered in greater detail. Finally, the likelihood of a fossil slab origin prompts questions about the physical and chemical evolution of a young oceanic plate translating with Pacific plate motion beneath the SAF system. As previously noted by Pikser et al. (2012), prolonged dehydration of the fossil slab and a possible serpentinized mantle wedge (Kirby et al., 2014) due to local isolation from the asthenosphere may provide an explanation for the limited along-strike extent of the creeping section of the SAF. However, coupled geodynamic and petrologic models of dehydration in subduction zones generally do not consider such atypical thermal regimes so the potential input of mantle volatiles at the base of the SAF due to a fossil slab remains uncertain.

5. Conclusions

We have imaged the Vs structure of the crust and upper mantle of central California with a cumulative data set including a new dense broadband array that filled in the least sampled areas above the Isabella Anomaly. The resulting images show that the Isabella Anomaly connects to a sub-horizontal high-Vs structure west of the Great Valley rather than the Sierra Nevada foothills to the east. The new tomography does support the Pliocene occurrence of lower crustal foundering beneath the high eastern Sierra Nevada. We conclude that a fossil slab origin for the Isabella Anomaly is more consistent with the imaged structure and that the foundered lithosphere from the eastern Sierra Nevada was likely smaller than the Isabella Anomaly and has either sunk through the asthenosphere or has a subtle velocity contrast. Interpretation of the Isabella Anomaly as fossil slab implies that during oblique ridge-trench collisions captured microplates can maintain slab fragments that extend into the upper mantle for >10 million years, and that these fragments may introduce along-strike variations in subsequent plate boundary deformation, such as the creeping section of the SAF.

Acknowledgements

Seismic data from the CCSE array will be openly available through the IRIS Data Management Center starting in November 2017. Deployment of the CCSE array would not have been possible without the support of private landowners and the Kern and Tulare County Fire Departments who hosted seismographs. Richard Guy is thanked for coordinating much of the fieldwork effort. Most of the seismographs used in the project were provided by the Tectonics Observatory at Caltech, which was funded by the Gordon and Betty Moore Foundation. Emily Brodsky and Elizabeth Cochran are thanked for loaning additional instruments. Emily Wolin, Will Levandowski, and Carl Tape are thanked for constructive reviews. Data collection and analysis were supported by NSF EAR 1315856 (BS), 1314910 (RWC), and CyberSEES-1442665 (FCL).

Appendix A. Supplementary material

Supplementary material related to this article can be found online at https://doi.org/10.1016/j.epsl.2018.02.009.

References

Atwater, T., Stock, J., 1998. Pacific-North America plate tectonics of the Neogene southwestern United States: an update. Int. Geol. Rev. 40 (5), 375–402.
Barak, S., Klemperer, S.L., Lawrence, J.F., 2015. San Andreas Fault dip, Peninsular Ranges mafic lower crust and partial melt in the Salton Trough, Southern California, from ambient-noise tomography. Geochem. Geophys. Geosyst. 16 (11), 3946–3972.
Barmin, M.P., Ritzwoller, M.H., Levshin, A.L., 2001. A fast and reliable method for surface wave tomography. Pure Appl. Geophys. 158 (8), 1351–1375.
Becken, M., Ritter, O., Bedrosian, P.A., Weckmann, U., 2011. Correlation between deep fluids, tremor and creep along the central San Andreas fault. Nature 480 (7375), 87.
Bensen, G.D., Ritzwoller, M.H., Barmin, M.P., Levshin, A.L., Lin, F., Moschetti, M.P., Shapiro, N.M., Yang, Y., 2007. Processing seismic ambient noise data to obtain reliable broad-band surface wave dispersion measurements. Geophys. J. Int. 169 (3), 1239–1260.
Benz, H.M., Zandt, G., 1993. Teleseismic tomography: lithospheric structure of the San Andreas fault system in northern and central California. In: Iyer, H.M., Hirahara, K. (Eds.), Seismic Tomography: Theory and Practice. Chapman and Hall, London, pp. 440–465.
Biasi, G.P., Humphreys, E.D., 1992. P-wave image of the upper mantle structure of central California and southern Nevada. Geophys. Res. Lett. 19 (11), 1161–1164.
Bodin, T., Sambridge, M., Tkalčić, H., Arroucau, P., Gallagher, K., Rawlinson, N., 2012. Transdimensional inversion of receiver functions and surface wave dispersion. J. Geophys. Res., Solid Earth 117 (B2). https://doi.org/10.1029/2011JB008560.
Boyd, O.S., Jones, C.H., Sheehan, A.F., 2004. Foundering lithosphere imaged beneath the southern Sierra Nevada, California, USA. Science 305 (5684), 660–662.
Brocher, T.M., Brink, U.S.T., Abramovitz, T., 1999. Synthesis of crustal seismic structure and implications for the concept of a slab gap beneath coastal California. Int. Geol. Rev. 41 (3), 263–274.
Brocher, T.M., 2005. Empirical relations between elastic wavespeeds and density in the Earth's crust. Bull. Seismol. Soc. Am. 95 (6), 2081–2092.
Burkett, E.R., Billen, M.I., 2009. Dynamics and implications of slab detachment due to ridge-trench collision. J. Geophys. Res., Solid Earth 114 (B12). https://doi.org/10.1029/2009JB006402.
Chu, R., Helmberger, D.V., Sun, D., Jackson, J.M., Zhu, L., 2010. Mushy magma beneath Yellowstone. Geophys. Res. Lett. 37, L01306. https://doi.org/10.1029/2009GL041656.

Chu, R., Schmandt, B., Helmberger, D.V., 2012. Juan de Fuca subduction zone from a mixture of tomography and waveform modeling. J. Geophys. Res., Solid Earth 117, B03304. https://doi.org/10.1029/2012JB009146.

Clark, M.K., Maheo, G., Saleeby, J., Farley, K.A., 2005. The non-equilibrium landscape of the southern Sierra Nevada, California. GSA Today 15 (9), 4.

Cox, P., Stubailo, I., Davis, P., 2016. Receiver function and geometric tomography along the monterey microplate to test slab delamination or lithospheric drip models of the Isabella Anomaly, California. Bull. Seismol. Soc. Am. 106 (1), 267–280.

Dickinson, W.R., 2008. Accretionary Mesozoic–Cenozoic expansion of the Cordilleran continental margin in California and adjacent Oregon. Geosphere 4 (2), 329–353.

Dougherty, S.L., Clayton, R.W., Hansen, S.M., Schmandt, B., 2017. Lithospheric structure in central California across the Isabella anomaly and tectonic implications. Seismol. Res. Lett. 88 (2B), 605–606. https://doi.org/10.1785/0220170035.

Ducea, M.N., Kidder, S., Zandt, G., 2003. Arc composition at mid-crustal depths: insights from the Coast Ridge Belt, Santa Lucia Mountains, California. Geophys. Res. Lett. 30 (13), 1703. https://doi.org/10.1029/2002GL016297.

Ducea, M.N., Saleeby, J.B., 1996. Buoyancy sources for a large, unrooted mountain range, the Sierra Nevada, California: evidence from xenolith thermobarometry. J. Geophys. Res., Solid Earth 101 (B4), 8229–8244.

Dziewonski, A.M., Anderson, D.L., 1981. Preliminary reference Earth model. Phys. Earth Planet. Inter. 25 (4), 297–356.

Fliedner, M.M., Klemperer, S.L., Christensen, N.I., 2000. Three-dimensional seismic model of the Sierra Nevada arc, California, and its implications for crustal and upper mantle composition. J. Geophys. Res., Solid Earth 105 (B5), 10899–10921.

Farmer, G.L., Glazner, A.F., Manley, C.R., 2002. Did lithospheric delamination trigger late Cenozoic potassic volcanism in the southern Sierra Nevada, California? Geol. Soc. Am. Bull. 114 (6), 754–768.

Ford, H.A., Fischer, K.M., Lekic, V., 2014. Localized shear in the deep lithosphere beneath the San Andreas fault system. Geology 42 (4), 295–298.

Forsyth, D.W., Li, A., 2005. Array analysis of two-dimensional variations in surface wave phase velocity and azimuthal anisotropy in the presence of multipathing interference. In: Seismic Earth: Array Analysis of Broadband Seismograms, pp. 81–97.

Frassetto, A.M., Zandt, G., Gilbert, H., Owens, T.J., Jones, C.H., 2011. Structure of the Sierra Nevada from receiver functions and implications for lithospheric foundering. Geosphere 7 (4), 898–921.

Fulton, P.M., Saffer, D.M., 2009. Potential role of mantle-derived fluids in weakening the San Andreas Fault. J. Geophys. Res., Solid Earth 114, B07408. https://doi.org/10.1029/2008JB006087.

Gilbert, H., Yang, Y., Forsyth, D.W., Jones, C.H., Owens, T.J., Zandt, G., Stachnik, J.C., 2012. Imaging lithospheric foundering in the structure of the Sierra Nevada. Geosphere 8 (6), 1310–1330.

Gilbert, H., 2012. Crustal structure and signatures of recent tectonism as influenced by ancient terranes in the western United States. Geosphere 8 (1), 141–157.

Godfrey, N.J., Klemperer, S.L., 1998. Ophiolitic basement to a forearc basin and implications for continental growth: the Coast Range/Great Valley ophiolite, California. Tectonics 17 (4), 558–570.

Hansen, S.M., Schmandt, B., Dougherty, S.L., Clayton, R.W., 2016. Interrogating the Isabella Anomaly with the Central California Seismic Array. In: AGU Fall Meeting Abstracts.

Herrmann, R.B., 2013. Computer programs in seismology: an evolving tool for instruction and research. Seismol. Res. Lett. 84 (6), 1081–1088.

Hickman, Stephen, Zoback, Mark, 2004. Stress orientations and magnitudes in the SAFOD pilot hole. Geophys. Res. Lett. 31 (15).

Holbrook, W.S., Mooney, W.D., 1987. The crustal structure of the axis of the Great Valley, California, from seismic refraction measurements. Tectonophysics 140 (1), 49–63.

Jagoutz, O., Kelemen, P.B., 2015. Role of arc processes in the formation of continental crust. Annu. Rev. Earth Planet. Sci. 43, 363–404.

Jiang, C., Yang, Y., Zheng, Y., 2014. Penetration of mid-crustal low velocity zone across the Kunlun Fault in the NE Tibetan Plateau revealed by ambient noise tomography. Earth Planet. Sci. Lett. 406, 81–92.

Jones, C.H., Reeg, H., Zandt, G., Gilbert, H., Owens, T.J., Stachnik, J., 2014. P-wave tomography of potential convective downwellings and their source regions, Sierra Nevada, California. Geosphere 10 (3), 505–533.

Julia, J., Ammon, C.J., Herrmann, R.B., Correig, A.M., 2000. Joint inversion of receiver function and surface wave dispersion observations. Geophys. J. Int. 143 (1), 99–112.

Kanamori, H., Anderson, D.L., 1977. Importance of physical dispersion in surface wave and free oscillation problems. Rev. Geophys. 15 (1), 105–112.

Kay, R.W., Kay, S.M., 1993. Delamination and delamination magmatism. Tectonophysics 219 (1–3), 177–189.

Kennedy, B.M., Kharaka, Y.K., Evans, W.C., Ellwood, A., DePaolo, D.J., Thordsen, J., Ambats, G., Mariner, R.H., 1997. Mantle fluids in the San Andreas fault system, California. Science 278 (5341), 1278–1281.

Kennett, B.L.N., Engdahl, E.R., Buland, R., 1995. Constraints on seismic velocities in the Earth from traveltimes. Geophys. J. Int. 122 (1), 108–124.

Kirby, S.H., Wang, K., Brocher, T.M., 2014. A large mantle water source for the northern San Andreas fault system: a ghost of subduction past. Earth Planets Space 66 (1), 67. https://doi.org/10.1186/1880-5981-66-67.

Kreemer, C., Hammond, W.C., 2007. Geodetic constraints on areal changes in the Pacific–North America plate boundary zone: what controls Basin and Range extension? Geology 35 (10), 943–946.

Lee, C.T., Rudnick, R.L., Brimhall, G.H., 2001. Deep lithospheric dynamics beneath the Sierra Nevada during the Mesozoic and Cenozoic as inferred from xenolith petrology. Geochem. Geophys. Geosyst. 2 (12). https://doi.org/10.1029/2001GC000152.

Lee, E.J., Chen, P., Jordan, T.H., Maechling, P.B., Denolle, M.A., Beroza, G.C., 2014. Full-3-D tomography for crustal structure in southern California based on the scattering-integral and the adjoint-wavefield methods. J. Geophys. Res., Solid Earth 119 (8), 6421–6451.

Le Pourhiet, L., Gurnis, M., Saleeby, J., 2006. Mantle instability beneath the Sierra Nevada mountains in California and Death Valley extension. Earth Planet. Sci. Lett. 251 (1), 104–119.

Le Pourhiet, L., Saleeby, J., 2013. Lithospheric convective instability could induce creep along part of the San Andreas fault. Geology 41 (9), 999–1002.

Levandowski, W., Jones, C.H., 2015. Linking Sierra Nevada, California, uplift to subsidence of the Tulare basin using a seismically derived density model. Tectonics 34 (11), 2349–2358.

Levandowski, W., Jones, C.H., Reeg, H., Frassetto, A., Gilbert, H., Zandt, G., Owens, T.J., 2013. Seismological estimates of means of isostatic support of the Sierra Nevada. Geosphere 9 (6), 1552–1561.

Levshin, A.L., Ritzwoller, M.H., 2001. Automated detection, extraction, and measurement of regional surface waves. In: Monitoring the Comprehensive Nuclear-Test-Ban Treaty: Surface Waves. Birkhäuser, Basel, pp. 1531–1545.

Lin, F.C., Moschetti, M.P., Ritzwoller, M.H., 2008. Surface wave tomography of the western United States from ambient seismic noise: Rayleigh and Love wave phase velocity maps. Geophys. J. Int. 173 (1), 281–298.

Lin, F.C., Tsai, V.C., Schmandt, B., 2014. 3-D crustal structure of the western United States: application of Rayleigh-wave ellipticity extracted from noise cross-correlations. Geophys. J. Int. 198 (2), 656–670.

Lockner, D.A., Morrow, C., Moore, D., Hickman, S., 2011. Low strength of deep San Andreas fault gouge from SAFOD core. Nature 472, 82–85. https://doi.org/10.1038/nature09927.

Lonsdale, P., 1991. Structural patterns of the Pacific floor offshore of peninsular California. In: The Gulf and Peninsular Province of the Californias, vol. 47, pp. 87–125.

Meltzer, A.S., Levander, A.R., 1991. Deep crustal reflection profiling offshore southern central California. J. Geophys. Res., Solid Earth 96 (B4), 6475–6491.

Mosegaard, K., Tarantola, A., 1995. Monte Carlo sampling of solutions to inverse problems. J. Geophys. Res., Solid Earth 100 (B7), 12431–12447.

Miller, K.C., Mooney, W.D., 1994. Crustal structure and composition of the southern Foothills Metamorphic Belt, Sierra Nevada, California, from seismic data. J. Geophys. Res., Solid Earth 99 (B4), 6865–6880.

Moore, D.E., Rymer, M.J., 2007. Talc-bearing serpentinite and the creeping section of the San Andreas fault. Nature 448, 795–797. https://doi.org/10.1038/nature06064.

Nicholson, C., Sorlien, C.C., Atwater, T., Crowell, J.C., Luyendyk, B.P., 1994. Microplate capture, rotation of the western Transverse Ranges, and initiation of the San Andreas transform as a low-angle fault system. Geology 22 (6), 491–495.

Obrebski, M., Allen, R.M., Pollitz, F., Hung, S.H., 2011. Lithosphere–asthenosphere interaction beneath the western United States from the joint inversion of body-wave traveltimes and surface-wave phase velocities. Geophys. J. Int. 185 (2), 1003–1021.

Panning, M., Romanowicz, B., 2006. A three-dimensional radially anisotropic model of shear velocity in the whole mantle. Geophys. J. Int. 167 (1), 361–379.

Paige, C.C., Saunders, M.A., 1982. LSQR: an algorithm for sparse linear equations and sparse least squares. ACM Trans. Math. Softw. 8 (1), 43–71.

Peng, Z., Vidale, J.E., Wech, A.G., Nadeau, R.M., Creager, K.C., 2009. Remote triggering of tremor along the San Andreas Fault in central California. J. Geophys. Res., Solid Earth 114, B00A06. https://doi.org/10.1029/2008JB006049.

Pikser, J.E., Forsyth, D.W., Hirth, G., 2012. Along-strike translation of a fossil slab. Earth Planet. Sci. Lett. 331, 315–321.

Provost, Ann-Sophie, Houston, Heidi, 2001. Orientation of the stress field surrounding the creeping section of the San Andreas fault: evidence for a narrow mechanically weak fault zone. J. Geophys. Res., Solid Earth 106 (B6), 11373–11386.

Raikes, S.A., 1980. Regional variations in upper mantle structure beneath southern California. Geophys. J. Int. 63 (1), 187–216.

Saleeby, J., Sharp, W., 1980. Chronology of the structural and petrologic development of the southwest Sierra Nevada foothills, California: summary. Geol. Soc. Am. Bull. 91 (6), 317–320.

Saleeby, J., 2007. The western extent of the Sierra Nevada batholith in the Great Valley basement and its significance in underlying mantle dynamics. In: AGU Fall Meeting Abstracts.

Saleeby, J., Foster, Z., 2004. Topographic response to mantle lithosphere removal in the southern Sierra Nevada region, California. Geology 32 (3), 245–248.

Schmandt, B., Humphreys, E., 2010a. Seismic heterogeneity and small-scale convection in the southern California upper mantle. Geochem. Geophys. Geosyst. 11, Q05004. https://doi.org/10.1029/2010GC003042.

Schmandt, B., Humphreys, E., 2010b. Complex subduction and small-scale convection revealed by body-wave tomography of the western United States upper mantle. Earth Planet. Sci. Lett. 297 (3), 435–445.

Schmandt, B., Lin, F.C., Karlstrom, K.E., 2015. Distinct crustal isostasy trends east and west of the Rocky Mountain Front. Geophys. Res. Lett. 42, 10290–10298. https://doi.org/10.1002/2015GL066593.

Seats, K.J., Lawrence, J.F., Prieto, G.A., 2012. Improved ambient noise correlation functions using Welch's method. Geophys. J. Int. 188 (2), 513–523.

Seccia, D., Chiarabba, C., De Gori, P., Bianchi, I., Hill, D.P., 2011. Evidence for the contemporary magmatic system beneath Long Valley Caldera from local earthquake tomography and receiver function analysis. J. Geophys. Res., Solid Earth 116, B12314. https://doi.org/10.1029/2011JB008471.

Shelly, D.R., Ellsworth, W.L., Ryberg, T., Haberland, C., Fuis, G.S., Murphy, J., Nadeau, R.M., Bürgmann, R., 2009. Precise location of San Andreas fault tremors near Cholame, California using seismometer clusters: slip on the deep extension of the fault? Geophys. Res. Lett. 36, L01303. https://doi.org/10.1029/2008GL036367.

Shelly, D.R., 2015. Complexity of the deep San Andreas Fault zone defined by cascading tremor. Nat. Geosci. 8 (2), 145–151. https://doi.org/10.1038/ngeo2335.

Shen, W., Ritzwoller, M.H., Schulte-Pelkum, V., Lin, F.C., 2013a. Joint inversion of surface wave dispersion and receiver functions: a Bayesian Monte-Carlo approach. Geophys. J. Int. 192 (2), 807–836.

Shen, W., Ritzwoller, M.H., Schulte-Pelkum, V., 2013b. A 3-D model of the crust and uppermost mantle beneath the Central and Western US by joint inversion of receiver functions and surface wave dispersion. J. Geophys. Res., Solid Earth 118 (1), 262–276.

Sousa, F.J., Saleeby, J., Farley, K.A., Unruh, J.R., Lloyd, M.K., 2017. The southern Sierra Nevada pediment, central California. Geosphere 13 (1), 82–101.

Tape, C., Plesch, A., Shaw, J.H., Gilbert, H., 2012. Estimating a continuous Moho surface for the California unified velocity model. Seismol. Res. Lett. 83 (4), 728–735.

Thomas, A.M., Nadeau, R.M., Bürgmann, R., 2009. Tremor-tide correlations and near-lithostatic pore pressure on the deep San Andreas fault. Nature 462, 1048–1051. https://doi.org/10.1038/nature08654.

Titus, S.J., DeMets, C., Tikoff, B., 2006. Thirty-five-year creep rates for the creeping segment of the San Andreas fault and the effects of the 2004 Parkfield earthquake: constraints from alignment arrays, continuous global positioning system, and creepmeters. Bull. Seismol. Soc. Am. 96 (4B), S250–S268.

Tréhu, A., 1991. Tracing the subducted oceanic crust beneath the central California continental margin: results from ocean bottom seismometers deployed during the 1986 Pacific Gas and Electric EDGE experiment. J. Geophys. Res., Solid Earth 96 (B4), 6493–6506.

Valera, J.L., Negredo, A.M., Billen, M.I., Jiménez-Munt, I., 2014. Lateral migration of a foundering high-density root: insights from numerical modeling applied to the southern Sierra Nevada. Lithos 189, 77–88.

VanDecar, J.C., Crosson, R.S., 1990. Determination of teleseismic relative phase arrival times using multi-channel cross-correlation and least squares. Bull. Seismol. Soc. Am. 80 (1), 150–169.

Wang, Y., Forsyth, D.W., Rau, C.J., Carriero, N., Schmandt, B., Gaherty, J.B., Savage, B., 2013. Fossil slabs attached to unsubducted fragments of the Farallon plate. Proc. Natl. Acad. Sci. 110 (14), 5342–5346.

Watanabe, T., 1993. Effects of water and melt on seismic velocities and their application to characterization of seismic reflectors. Geophys. Res. Lett. 20 (24), 2933–2936.

Wernicke, B., Clayton, R., Ducea, M., Jones, C.H., Park, S., Ruppert, S., Saleeby, J., Snow, J.K., Squires, L., Fliedner, M., Jiracek, G., Keller, R., Klemperer, S., Luetgert, J., Malin, P., Miller, K., Mooney, W., Oliver, H., Phinney, R., 1996. Origin of high mountains in the continents: the southern Sierra Nevada. Science 271 (5246), 190–192.

Wilson, D.S., McCrory, P.A., Stanley, R.G., 2005. Implications of volcanism in coastal California for the Neogene deformation history of western North America. Tectonics 24, TC3008. https://doi.org/10.1029/2003TC001621.

Xing, G., Niu, F., Chen, M., Yang, Y., 2016. Effects of shallow density structure on the inversion for crustal shear wave speeds in surface wave tomography. Geophys. J. Int. 205 (2), 1144–1152.

Yang, Y., Forsyth, D.W., 2006a. Regional tomographic inversion of the amplitude and phase of Rayleigh waves with 2-D sensitivity kernels. Geophys. J. Int. 166 (3), 1148–1160.

Yang, Y., Forsyth, D.W., 2006b. Rayleigh wave phase velocities, small-scale convection, and azimuthal anisotropy beneath southern California. J. Geophys. Res., Solid Earth 111, B07306. https://doi.org/10.1029/2005JB004180.

Yao, H., Van Der Hilst, R.D., Montagner, J.P., 2010. Heterogeneity and anisotropy of the lithosphere of SE Tibet from surface wave array tomography. J. Geophys. Res., Solid Earth 115, B12307. https://doi.org/10.1029/2009JB007142.

Zandt, G., 2003. The southern Sierra Nevada drip and the mantle wind direction beneath the southwestern United States. Int. Geol. Rev. 45 (3), 213–224.

Zandt, G., Hersh, G., Owens, T.J., Ducea, M., Saleeby, J., Jones, C.H., 2004. Active foundering of a continental arc root beneath the southern Sierra Nevada in California. Nature 431, 41–46. https://doi.org/10.1038/nature02847.

Zhang, H., Maceira, M., Roux, P., Thurber, C., 2014. Joint inversion of body-wave arrival times and surface-wave dispersion for three-dimensional seismic structure around SAFOD. Pure Appl. Geophys. 171 (11), 3013–3022.

Zhou, Y., Dahlen, F.A., Nolet, G., 2004. Three-dimensional sensitivity kernels for surface wave observables. Geophys. J. Int. 158 (1), 142–168.